

Three-dimensional two-layer outer gap model: *Fermi* energy-dependent light curves of the Vela pulsar

Y. Wang,^{*} J. Takata^{*} and K. S. Cheng^{*}

Department of Physics, University of Hong Kong, Pokfulam Road, Hong Kong

Accepted 2011 February 21. Received 2011 February 21; in original form 2011 January 7

ABSTRACT

We extend the two-dimensional two-layer outer gap model to a three-dimensional geometry and use it to study the high-energy emission of the Vela pulsar. In this model, the outer gap is divided into two parts, i.e. the main acceleration region on the top of last-open field lines and the screening region around the upper boundary of the gap. In the main acceleration region, the charge density is much lower than the Goldreich–Julian charge density, and the charged particles are accelerated by the electric field along the magnetic field to emit multi-GeV photons. In the screening region, the charge density is larger than the Goldreich–Julian value to close the gap, and particles in this region are responsible for multi-100 MeV photon emission. We apply this three-dimensional two-layer model to the Vela pulsar and compare the model light curves, the phase-averaged spectrum and the phase-resolved spectra with the recent *Fermi* observations, which also reveals the existence of the third peak between two main peaks. The phase position of the third peak moves with the photon energy, which cannot be explained by the geometry of magnetic field structure and the caustic effects of the photon propagation. We suggest that the existence of the third peak and its energy-dependent movement results from the azimuthal structure of the outer gap.

Key words: radiation mechanisms: non-thermal – methods: numerical – pulsars: general.

1 INTRODUCTION

The Vela pulsar is one of the few γ -ray pulsars whose γ -ray radiations are so intense that could be detected before the launch of the *Fermi* γ -ray telescopes. For this reason, the observed spectra and the pulse profiles of the Vela pulsar have been studied extensively before the launch of the *Fermi* (Romani 1996; Dyks, Harding & Rudak 2004; Takata, Chang & Shibata 2008). Its γ -ray spectrum between 100 MeV to several GeV is difficult to be explained in terms of simple curvature radiation. Takata et al. (2008) proposed that the component around 100 MeV of the Vela pulsar, as well as Geminga (Takata & Chang 2009), is due to the synchrotron radiation of the incoming particles in the outer gap. By solving the evolution of the Lorentz factor and the pitch angle in the two-dimensional electro-dynamics model (Takata, Shibata & Hirotani 2004), they found that the synchrotron radiation of the incoming particles dominates the radiation around 10–100 MeV, and the curvature radiation of the outgoing particles dominates the radiation around 1 GeV.

Zhang & Cheng (1997) proposed a self-sustained thick outer gap model of γ -ray emission from the rotation-powered pulsar. They

pointed out that the primary e^\pm pairs in the steady state have a power-law distribution and used this distribution to calculate the spectra of some γ -ray pulsars, including Geminga-like and Vela-like pulsars. Also based on this distribution of primary pairs, Zhang & Cheng (2001) applied a three-dimensional pulsar magnetosphere model to explain the high-energy emission from the Geminga pulsar with a thick outer gap. In this calculation, the high-energy γ -rays are produced by the accelerated particles with a power-law energy distribution via curvature radiation inside the outer gap.

After the launch of the *Fermi*-Large Area Telescope (LAT), the bottleneck of the research of high-energy radiation from pulsar is broken. Just in one year, this high-quality γ -ray telescope has measured 46 γ -ray pulsars (Abdo et al. 2010a). We developed a two-layer model (Wang, Takata & Cheng 2010) to study the phase-averaged spectra of the mature pulsars, including the Vela pulsar, in the first catalogue of γ -ray pulsars of the *Fermi*. In this simple two-dimensional model, the outer gap extending outwards from the null charge surface is considered as a superposition of a main acceleration region and a screening region. In the main acceleration region, which is close to vacuum, the electric field is strong, and the photons generated in this region dominate the radiation of around GeV range. In the screening region, the large numbers of the pairs produced by the pair-creation process stop the growth of the acceleration region, and they produce the photons

^{*}E-mail: yuwang@hku.hk (YW); takata@hku.hk (JT); hrspksc@hkucc.hku.hk (KSC)

with around 100 MeV range. Although this two-dimensional two-layer model could explain the phase-average γ -ray spectra of the mature pulsars, it cannot be used to study the phase-resolved spectra and the light curves. Furthermore, the high-quality data of the *Fermi* have clearly shown the existence of a third peak (bump) at the trailing part of the first peak, which was explained as an effect of geometry of the magnetic field (Dyks & Rudak 2003; Fang & Zhang 2010). However, the observed result provided by the *Fermi* (Abdo et al. 2010b) shows that, as the energy increases, this third peak shifts towards the second peak. This indicates that unlike those two main peaks this third peak does not result from the caustic effect of photon propagation and/or the structure of the magnetic field.

The high-energy radiation processes of pulsars have been studied based on polar cap models (Ruderman & Sutherland 1975; Daugherty & Harding 1982), the slot gap models (Arons 1983; Harding, Usov & Muslimov 2005; Harding et al. 2008), the annular gap model (Du et al. 2011) and the outer gap models (Cheng, Ho & Ruderman 1986a,b; Romani 1996; Hirovani 2008; Takata & Chang 2009). The different acceleration models have predicted different properties of the γ -ray emission properties from the pulsar magnetosphere. To discriminate among these existed emission models, it is better to compare the predicted phase-resolved spectra with the observed ones, which contain the most detailed information about the structure of pulsar magnetosphere and the acceleration mechanism.

In this paper, we extend our study of two-layer model from two-dimensional to three-dimensional, which includes the effects of the inclination angle, viewing angle and the azimuthal structure of the gap. This three-dimensional model can provide the phase-resolved spectra and the energy-dependent light curves that cannot be given by the two-dimensional one. We will use it to study the observed energy-dependent light curves of the Vela pulsar measured by the *Fermi*-LAT (Abdo et al. 2010b).

In Section 2, we describe our theoretical model, which contains the electrodynamics of the outer gap, the emission geometry and the method to calculate the spectra and the light curves. In Section 3, we will use our three-dimensional model to explain the energy-dependent light curves of the Vela pulsar and discuss the conditions of the existence and the movement of the third peak as well as other observed spectral properties. A brief summary is given in Section 4.

2 THEORETICAL MODEL

2.1 Three-dimensional gap structure

We discuss the γ -ray emissions from the outer gap accelerator in the pulsar magnetosphere, and assume that a strong acceleration region is extending above the last-open field lines and between the null charge surface of the Goldreich–Julian charge density and the light cylinder. Although the dynamical studies (e.g. Takata et al. 2004) predict that the inner boundary of the active gap can extend inwards from the null charge surface, most of the power of the gap is released beyond the null charge surface. Because the pairs are always created on convex side of the magnetic field lines, the charge number density increases as the height measured from the last-open field lines. In the trans-field direction of the magnetic field, therefore, as shown in Fig. 1, the outer gap can be divided into two parts: (1) the main acceleration region at the lower part of the outer gap, where the charge density is assumed to be ~ 10 per cent of the Goldreich–Julian value and a strong electric field is accelerating the particles to emit GeV photons via the curvature process, and (2) the screening region around the upper boundary, where the growth of the main acceleration region in the trans-field direction

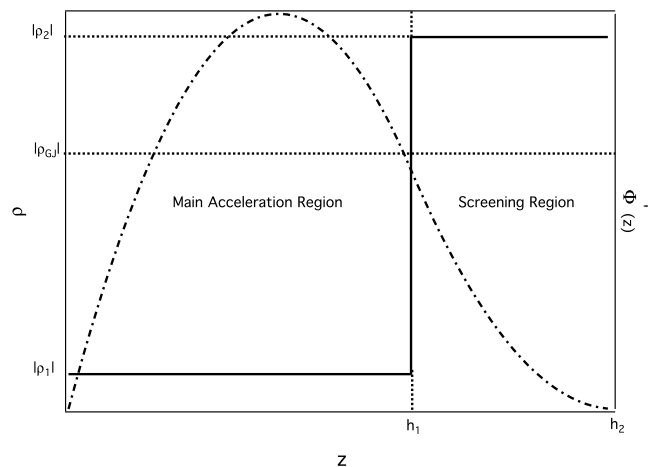


Figure 1. The simplified distribution of the charge density (solid line) and the corresponding accelerating potential (dot-dashed line) of the two-layer outer gap.

is stopped by the pair-creation process. Such two-layer structure, in the direction along the field line, starts from a place between the inner boundary and the null charge surface, and ends at the light cylinder. Inside the inner boundary and outside the light cylinder, there is no accelerating electric field; from the null charge surface to the inner boundary, the accelerating electric field decreases rapidly to zero.

Because the number density of the pairs made by the pair-creation process increases exponentially in the trans-field direction (Cheng et al. 1986a,b), we use a simple step function to approximate the distribution of the charge density in the trans-field direction in the poloidal plane (the plane where the field lines have same polar angle ϕ_p) as

$$\rho(x, z, \phi_p) = \begin{cases} \rho_1(x, \phi_p), & \text{if } 0 \leq z \leq h_1(x, \phi_p) \\ \rho_2(x, \phi_p), & \text{if } h_1(x, \phi_p) < z \leq h_2(x, \phi_p) \end{cases}, \quad (1)$$

where x , z and ϕ_p represent coordinates along the magnetic field line, the height measured from the last-open field line and the azimuthal direction. In addition, h_1 and h_2 represent the thickness of the main-accretion region and the total gap thickness, respectively. As illustrated in Fig. 1, in the z -direction, the main acceleration region spans from $z = 0$ to h_1 , where the charge density is substantially smaller than the Goldreich–Julian charge density (Goldreich & Julian 1969), and the screening region is between $h_1 \leq z \leq h_2$, the charge density in it is much higher than ρ_{GJ} in order to close the gap. For each poloidal plane ($\phi_p = \text{constant}$), $h_1(x, \phi_p)$ as well as $h_2(x, \phi_p)$ is defined with a given magnetic field line in the constant ϕ_p -plane so that the ratio $h_1(x, \phi_p)/h_2(x, \phi_p)$ is nearly constant along the field lines.

Even though the structure of the gap is simplified as described above, the three-dimensional Poisson equation with the magnetic field structure is still difficult to be solved in comparing with the case of the two-dimensional model discussed in Wang et al. (2010). Instead of solving the real three-dimensional Poisson equation, we adopt a simplified Poisson equation. We calculate the electric field structure at a fixed poloidal plane, that is, at each azimuthal coordinate by solving the two-dimensional Poisson equation. This approximation can be justified if the derivation of the potential field in the azimuthal direction is much smaller than that in poloidal plane. This procedure may be applicable for the thin outer gap accelerator, whose thickness in the poloidal plane is much smaller

than the width in the azimuthal direction. The detail procedure to obtain the three-dimensional structure is described as follows.

In a fixed poloidal plane, the bottom and top boundaries of the outer gap are the last-open field lines and a surface layer with separation h_2 made by the magnetic field lines, respectively. We divide the polar cap into N_B equal divisions in the azimuthal direction. If the gap size of the azimuthal direction is much larger than the gap thickness in the poloidal plane, the gap structure of each slice with a fixed azimuthal angle ϕ_p may be approximately represented by the two-dimensional situation shown in Wang et al. (2010).

The accelerating electric field in each slice of the gap is solved by the method described in the previous two-dimensional model (Wang et al. 2010). The potential in the gap is described by the Poisson equation, $\nabla^2\Phi = -4\pi\rho$. This potential can be written as $\Phi = \Phi' + \Phi_0$, where Φ_0 is the corotating potential, which satisfies $\nabla^2\Phi_0 = -4\pi\rho_{\text{GJ}}$, and the potential Φ' represents the deviation from corotating potential. This deviation generates the accelerating electric field. By assuming the derivation of the potential field in the azimuthal direction is small enough to be neglected compared with that in the poloidal plane, we express the Poisson equation of Φ' as

$$\left(\frac{\partial^2}{\partial x^2} + \frac{\partial^2}{\partial z^2}\right)\Phi' = -4\pi(\rho - \rho_{\text{GJ}}). \quad (2)$$

Because our two-dimensional study predicts that the outer gap of the Vela pulsar is thin, the variation of the Goldreich–Julian charge density in the trans-field direction (that is z -direction) may be able to be neglected so that the ρ_{GJ} can be assumed to be constant in z -direction.

Moreover, we assume that the derivative of the potential field in the trans-field (z) direction is larger than that along (x -direction) the magnetic field line. This assumption may be applicable for the thin outer gap accelerator of the Vela pulsar. By ignoring the derivative of the potential field along the magnetic field line, we reduce the two-dimensional Poisson equation (2) to one-dimensional form as

$$\frac{\partial^2}{\partial z^2}\Phi'(x, z, \phi_p) = -4\pi[\rho(x, z, \phi_p) - \rho_{\text{GJ}}(x, \phi_p)]. \quad (3)$$

At the lower boundary, where the accelerating electric field just begins, the boundary condition is

$$\Phi'(x, z = 0, \phi_p) = 0. \quad (4)$$

At the upper boundary, which is located on the surface of fixed magnetic field line, we impose

$$\Phi'(x, z = h_2, \phi_p) = 0 \quad \text{and} \quad E_{\perp}(x, z = h_2, \phi_p) = 0. \quad (5)$$

Using the above boundary conditions and imposing that Φ' and $\partial\Phi'/\partial z$ are continuous at the height h_1 , we obtain the solution for the Poisson equation (3) as

$$\Phi'(x, z, \phi_p) = -2\pi \begin{cases} \{\rho_1(x, \phi_p) - \rho_{\text{GJ}}(x, \phi_p)\}z^2 \\ + C_1 z, \\ \text{for } 0 \leq z \leq h_1 \\ \{\rho_2(x, \phi_p) - \rho_{\text{GJ}}(x, \phi_p)\} \\ [z^2 - h_2^2(x, \phi_p)] \\ + D_1[z - h_2(x, \phi_p)], \\ \text{for } h_1 \leq z \leq h_2 \end{cases}, \quad (6)$$

where

$$C_1 = \frac{(\rho_1 - \rho_{\text{GJ}})h_1(h_1 - 2h_2) - (\rho_2 - \rho_{\text{GJ}})(h_1 - h_2)^2}{h_2},$$

$$D_1 = \frac{(\rho_{\text{GJ}} - \rho_2)h_2^2 + (\rho_1 - \rho_2)h_1^2}{h_2}.$$

Because the two boundary conditions are imposed on the upper boundary ($z = h_2$), the position of the upper boundary cannot be chosen arbitrarily. On the other hand, the condition $E_{\perp}(x, z = h_2, \phi_p) = 0$ gives the relation between the charge densities (ρ_1, ρ_2) and the gap thickness (h_1, h_2) as

$$(\rho_2 - \rho_{\text{GJ}})h_2^2 + (\rho_1 - \rho_2)h_1^2 = 0. \quad (7)$$

The present model expects that the charge density should proportional to the Goldreich–Julian charge density in the screening region (see Wang et al. 2010), and therefore we express $\rho(x, z, \phi_p) - \rho_{\text{GJ}}(x, \phi_p) \sim g(z, \phi_p)\rho_{\text{GJ}}(x, \phi_p)$, where

$$g(z, \phi_p) = \begin{cases} -g_1(\phi_p), & \text{if } 0 \leq z \leq h_1 \\ g_2(\phi_p), & \text{if } h_1 < z \leq h_2 \end{cases}. \quad (8)$$

We assume that $g_1 > 0$ and $g_2 > 0$ so that $|\rho| < |\rho_{\text{GJ}}|$ in the main region and $|\rho| > |\rho_{\text{GJ}}|$ for the screening region, respectively. Substituting equation (8) into equation (7), we obtain

$$\left(\frac{h_2}{h_1}\right)^2 = 1 + \frac{g_1}{g_2}. \quad (9)$$

We approximate that the Goldreich–Julian charge density as $\rho_{\text{GJ}}(x) \approx -(\Omega Bx/2\pi cs)$ (Cheng, Ho Ruderman 1986a), where Ω is the angular frequency of the pulsar. Using the relations that $\partial(Bh_2^2)/\partial x \sim 0$, $\partial(z/h_2)/\partial x \sim 0$, $\partial(h_1/h_2)/\partial x \sim 0$ and $\partial s/\partial x \sim 0$, the accelerating electric field, $E_{\parallel} = -\partial\Phi'/\partial x$, is written down as

$$E_{\parallel}(x, z, \phi_p) \sim \frac{\Omega B}{cs} \begin{cases} -g_1 z^2 + C'_1 z, \\ \text{for } 0 \leq z \leq h_1 \\ g_2(z^2 - h_2^2) + D'_1(z - h_2), \\ \text{for } h_1 < z \leq h_2 \end{cases}, \quad (10)$$

where

$$C'_1 = -\frac{g_1 h_1(h_1 - 2h_2) + g_2(h_1 - h_2)^2}{h_2},$$

$$D'_1 = -\frac{g_2 h_2^2 + (g_1 + g_2)h_1^2}{h_2}.$$

In the three-dimensional rotating magnetic field structure, the thickness of the gap h_2 is a function of the distance to the star along the field line x . We define the gap fraction f measured on the stellar surface as (Takata, Wang & Cheng 2010)

$$f \equiv \frac{h_2(R_s)}{r_p}, \quad (11)$$

where R_s is the stellar radius, and $r_p(\phi_p)$ is the polar cap radius and depends on polar angle in three-dimensional magnetic field geometry. Note that because the electric field E_{\parallel} is proportional to Bh_2^2 , which is almost constant along the field line for the dipole field, it can be found that $E_{\parallel} \propto f^2$. This indicates that the strength of the electric field and resultant emissivity of the curvature radiation increase with the fractional gap thickness.

The height(z) measured from the last-open field lines is a function of distance (x) along the magnetic field line. In order to make it easy to distinguish the two layers in any x , we introduce the factor a to represent the magnetic field lines at a given layer and take $a = 1$ for the last-open field lines. We first determine the coordinate values [$X_0(\phi_p)$, $Y_0(\phi_p)$, $Z_0(\phi_p)$] of the last-open field lines at the stellar surface. Then an arbitrary layer of the magnetic field lines with a

given ‘ a ’, whose coordinate values $[X_0(\phi_p), Y_0(\phi_p), Z_0(\phi_p)]$, can be determined by using $X_0(\phi_p) = aX_0(\phi_p)$, $Y_0(\phi_p) = aY_0(\phi_p)$ and $Z_0(\phi_p) = (R_s^2 - a^2X_0'^2 - a^2Y_0'^2)^{1/2}$. The relation between the z and the a is approximated as

$$z(x, \phi_p) = \frac{1-a}{1-a_{\min}} h_2(x, \phi_p), \quad (12)$$

where a_{\min} corresponds to the upper boundary of the gap. In this paper, the dimensionless thickness a_{\min} is assumed to be the same for different polar angle ϕ_p because each layer should have a similar polar cap shape on the stellar surface, and is chosen as the fitting parameter of the light curve. The thickness a_{\min} determines the width of the pulse peaks and the phase separation between two main peaks.

2.2 Curvature radiation spectrum

Our calculation method for the phase-average spectrum and phase-resolved spectra is based on Tang Anisia et al. (2008). In a volume element ΔV , there are $\Delta N = \Delta V n$ particles accelerated by the electric field that is described by equation (10). The accelerated particles release the power gained from the accelerating electric field, $eE_{\parallel}c$, through the curvature radiation process. The total radiation power for each particle is $l_{\text{cur}}(\mathbf{r}) = 2e^2c\gamma_e^4(\mathbf{r})/3s^2(\mathbf{r})$, where $\mathbf{r} = (x, z, p)$. The typical local Lorentz factor γ_e of the primary particles can be obtained by requiring $eE_{\parallel}c = l_{\text{cur}}$, which gives

$$\gamma_e(\mathbf{r}) = \left[\frac{3s^2(\mathbf{r})}{2e} E_{\parallel}(\mathbf{r}) \right]^{1/4}. \quad (13)$$

The photon spectrum at each position of radiation is

$$\frac{d^2 N_{\gamma}(E_{\gamma}, \mathbf{r})}{dE_{\gamma} dt} = \frac{\Delta N(\mathbf{r}) \sqrt{3} e^2 \gamma_e}{2\pi \hbar s E_{\gamma}} F(\chi), \quad (14)$$

where $\chi = E_{\gamma}/E_{\text{cur}}(\mathbf{r})$, $E_{\text{cur}}(\mathbf{r}) = (3/2)\hbar c\gamma_e^3(\mathbf{r})/s(\mathbf{r})$ is the characteristic energy of the radiated curvature photons, $s(\mathbf{r})$ is curvature radius and $F(\chi) = \int_{\chi}^{\infty} K_{5/3}(\xi) d\xi$, where $K_{5/3}$ is the modified Bessel functions of order 5/3. The local solid angle of curvature photon $\Delta\Omega \simeq \pi\theta^2$, where

$$\theta(\mathbf{r}) = \text{Max}[\Delta l/s(\mathbf{r}), \gamma(\mathbf{r})mc^2/eB(\mathbf{r})s(\mathbf{r})], \quad (15)$$

where the first term represents the solid angle caused by the curvature of the magnetic field line and the second term is the minimum emission angle measured from the direction of the magnetic field line. Here Δl is the gird size of the cell along field line.

With equation (8), we express the number density at each point as $n(\mathbf{r}) = \frac{\Omega B}{2\pi c} [1 - g(z, \phi_p)]$. The volume element at each position can be calculated:

$$\Delta V(\mathbf{r}) = \frac{2\pi r_p h(R_s) B(R_s) \Delta l(x)}{N_A N_B B(\mathbf{r})}, \quad (16)$$

where $2\pi r_p h_2(R_s) B_s$ is the total magnetic flux through in the gap, and N_A and N_B are the number of the grids in the direction of the trans-field direction (z -direction) and the azimuthal direction, respectively.

The total photon flux received at Earth is

$$F_{\text{tot}}(E_{\gamma}) = \frac{1}{D^2} \sum_{r_i} \frac{1}{\Delta\Omega(r_i)} \frac{d^2 N_{\gamma}(E_{\gamma}, \mathbf{r}_i)}{dE_{\gamma} dt}, \quad (17)$$

where \mathbf{r}_i represents the position of the i th cell, from which the emission can be observed, and D is the distance to the pulsar from Earth. We note that because r_i depends on the viewing angle and

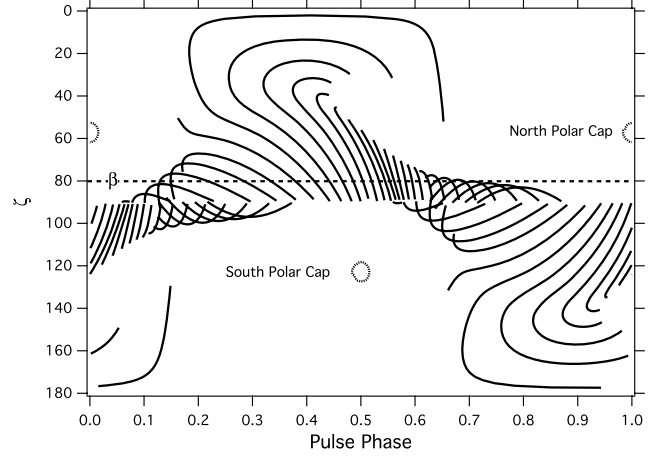


Figure 2. The sky-map of the radiations outside of the null charge surface with inclination angle $\alpha = 57^\circ$. The x -axis is the pulse phase and the y -axis is the direction of the radiation. The dashed line is the viewing angle, which is chosen as $\beta = 80^\circ$.

the inclination angle, the spectrum (17) is a function of the viewing angle and the inclination angle.

To calculate the phase-resolved spectra and the light curves, the arrival times of the photons are binned by pulse phase. For example, Fig. 2 represents photon-mapping on the plane spanned by the viewing angle and the pulse phase using the rotating dipole fields (Section 2.3). For each viewing angle, the number of the photons measured at pulse phases between ψ_1 and ψ_2 is calculated from

$$N_{\gamma}(E_1, E_2, \psi_1, \psi_2) \propto \int_{E_1}^{E_2} F_{\text{tot}}(E, \psi_1 \leq \psi \leq \psi_2) dE. \quad (18)$$

2.3 Emission geometry

It has been considered that the positions of the first and the second peaks of the pulsar are determined by the geometry of the magnetic field. In this study, we adopt the rotating vacuum dipole field to calculate the light curves and spectra. For the rotating dipole, the magnetic field $\mathbf{B}(\mathbf{r})$ is given by

$$\mathbf{B} = \hat{r} \left[\hat{r} \cdot \left(\frac{3\mu}{r^3} + \frac{3\dot{\mu}}{cr^2} + \frac{\ddot{\mu}}{c^2 r} \right) \right] - \left(\frac{\mu}{r^3} + \frac{\dot{\mu}}{cr^2} + \frac{\ddot{\mu}}{c^2 r} \right) \quad (19)$$

(Cheng, Ruderman & Zhang 2000), where $\dot{\mu} = \mu(\hat{x} \sin \alpha \cos \Omega t + \hat{y} \sin \alpha \sin \Omega t + \hat{z} \cos \alpha)$ is the magnetic moment vector, \hat{r} is the radial unit vector and α is the inclination angle. The Runge–Kutta method is employed to trace out field lines and to find the polar cap rim $[X_0(\phi_p), Y_0(\phi_p), Z_0(\phi_p)]$.

Once the upper boundary a_{\min} is chosen, we trace the open field lines defining the outer gap, and calculate the emission direction in the observer’s frame at each point on the field lines. In Tang Anisia et al. (2008), the emission direction coincides with the direction of the rotating vacuum dipole field defined in the corotating frame. In the present three-dimensional model, on the other hand, the emission direction calculated in only observer’s frame with the computation method employed by Takata et al. (2007). The curvature photons are assumed to be emitted in the direction of the particle motion, which can be described as

$$\mathbf{v} = v_p \mathbf{B}/B + \mathbf{r} \times \boldsymbol{\Omega}, \quad (20)$$

where the first term represents the motion along the magnetic field line, v_p is calculated from the condition that $|\mathbf{v}| = c$, and the second

term is the drift motion. The polar angle to the rotation axis ζ of the emission direction and the pulse phase ψ are calculated from

$$\begin{cases} \cos \zeta = v_z/v \\ \psi = -\cos^{-1}(v_x/v_{xy}) - \mathbf{r} \cdot \hat{\mathbf{v}}/R_L \end{cases} \quad (21)$$

(Yadigaroglu 1997). If a point in a field line satisfies $|\zeta - \beta| < \varphi(r)$, the radiation of that point can be seen by the observer, where β is the viewing angle and $\varphi(r) = \Delta l(r)/s(r)$. Because the positions of the first and second peaks in the light curve are also determined by viewing geometry, the predicted inclination angle α and the viewing angle β are uniquely determined by comparing the calculated peak separation with the observations.

3 RESULTS AND DISCUSSION

In this section, we apply our model to the Vela pulsar. In our two-layer model, the general properties of γ -ray emissions from the outer gap are characterized by f , g_1 and h_1/h_2 . Specifically, the gap fraction f mainly determines the cut-off energy in the spectrum. Zhang & Cheng (1997) suggested a self-consistent mechanism provided by the X-rays emitted by the polar cap that is heated by the return current to restrict the gap. Their fractional size of the gap, $f_{ZC} = 0.32P_{-1}^{26/21} B_{12}^{-4/7}$, predicts that of the Vela pulsar is 0.15. In the two-dimensional model (Wang et al. 2010), $f = 0.16$ was used for fitting the phase-averaged spectrum of the Vela pulsar. The current in the main acceleration region, $1 - g_1$, and the ratio between the thicknesses of the main acceleration region and that of the whole gap, h_1/h_2 , determine the photon index of the spectrum together. For the Vela pulsar, the fitting of the two-dimensional two-layer model gives $1 - g_1 = 0.08$ and $h_1/h_2 = 0.927$ (Wang et al. 2010).

The position of the upper boundary a_{\min} is treated as a model parameter, because it is affected by the actual magnetic field structure, which is not understood well. Together with the inclination angle α and the viewing angle β , the position of the upper boundary a_{\min} can be constrained by the detailed structure of pulsed profile. As we show in the following section, we find that the set of $(\alpha, \beta, a_{\min}) = (57^\circ, 80^\circ, 0.935)$ reproduces well both the light curves and the spectra. Fig. 2 shows the sky-map of the emitted photons from the magnetic surface of $a = 0.95$ with $\alpha = 57^\circ$ and $\beta = 80^\circ$. Although there are many sets of the inclination angle and the viewing angle that can provide the observed peak separation, our choice of these two angles is not arbitrary. The reason for this will be discussed later.

3.1 A simple case

First, we assume constant $1 - g_1, h_1/h_2$ and f in the azimuthal direction. By fitting the phase-averaged spectrum for the Vela pulsar, we obtain $1 - g_1 = 0.05, h_1/h_2 = 0.927$ and $f = 0.2$ for the present three-dimensional model. Here we assume the distance of $D = 325$ pc.

Fig. 3 compares the calculated (histograms) and the observed (solid lines) pulse profiles in six different energy bands. We can see in Fig. 3 that the model-provided pulse profiles are generally consistent with the observations. For example, the pulsed profiles in wide energy bands have two main peaks with the separation of about 0.42. The positions of the two peaks in the light curves are determined by the geometry of the magnetic field.

In the present simple model, however, the calculated pulse profile cannot explain the existence of the observed third peak between two main peaks, as we can see in Fig. 3. The peaks emerging in the

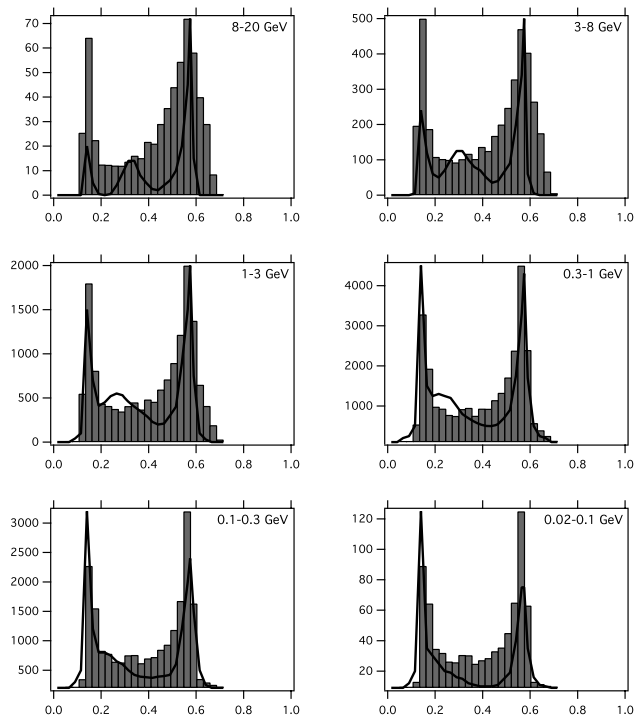


Figure 3. The energy-dependent light curves (histogram) with $1 - g_1 = 0.05, h_1/h_2 = 0.927$ and $f = 0.2$. The solid lines are the observed light curves from the *Fermi*-LAT (Abdo et al. 2010b). The y-axis is the counts of the observed light curve.

calculated pulse profiles of Fig. 3 are caused by so-called caustic effects (Yadigaroglu & Romani 1995; Cheng et al. 2000; Dyks et al. 2004), in which more photons are observed at narrow width of the rotation phase due to the special-relativistic effect (that is, the aberration of the emission direction and photon's travel time). In the caustic model, the phases of the peaks are determined by the magnetic field structure, and they do not depend on the energy band. On the other hand, the observed phase of the third peak shifts with the energy bands. The simple caustic model cannot explain the phase shift of the observed third peak. On these ground, we speculate that the existence of the third peak and its phase shift is related with more complex structure of the emission region.

3.2 More realistic case

In this section, we discuss the third peak with a more complex gap structure by taking into account the azimuthal structure of the fractional gap thickness f , the ratio of the thicknesses of the main acceleration region to the whole gap thickness, h_1/h_2 , and the particle number density in the main acceleration region, $1 - g_1$.

3.2.1 Fractional gap thickness

First, we consider the azimuthal structure of fractional gap thickness and compare the calculated light curves with the observations.

By the definition of the gap fraction of equation (11), $f \propto 1/r_p$, we may choose the form of the azimuthal distribution of f as

$$f(\phi_p) = \frac{C}{r_p(\phi_p)}, \quad (22)$$

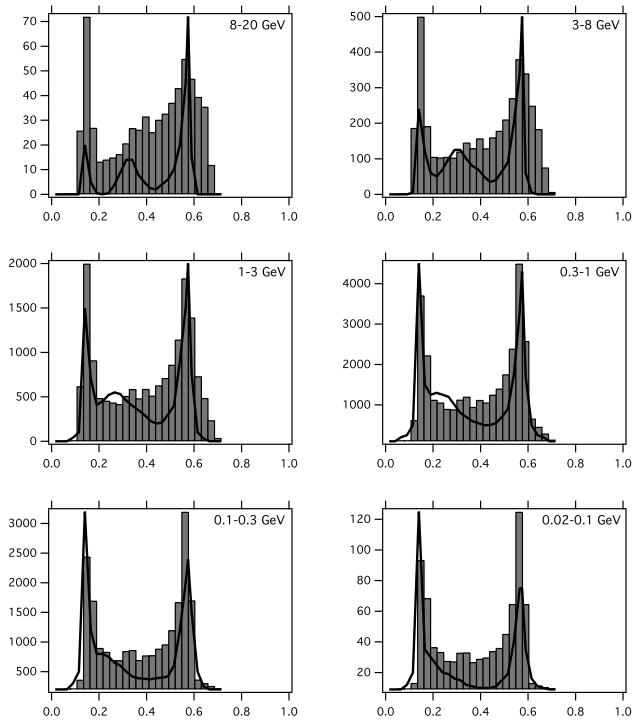


Figure 4. The energy-dependent light curves (histogram) with the distribution of f provided by the three-dimensional outer gap. $1 - g_1$ and h_1/h_2 are chosen as 0.05 and 0.927, respectively. The solid lines are the observed light curves from the *Fermi*-LAT (Abdo et al. 2010b).

where the $C = 0.18r_p^{\max}$, r_p^{\max} is the maximum value of the polar cap radius, and the factor 0.18 is chosen by fitting the phase-averaged spectrum.

The pulse profiles using the fractional thickness f described by equation (22) are shown in Fig. 4, where $g_1 = 0.05$ and $h_1/h_2 = 0.927$ are the same with those of Fig. 3. By comparing Figs 3 and 4, we can find the effects of azimuthal distribution of f on the pulse profile. For example, the azimuthal structure of the fractional gap thickness produces more bridge emissions as well as a third-peak-like feature at the phase ~ 0.3 of the pulse profile (in particular, for higher energy bands) in Fig. 4.

Fig. 5 shows the polar cap radius r_p (solid line) and the resultant fractional gap thickness f (dashed line) as a function of the polar angle. The polar angle $= 0^\circ$ is defined at the right-hand side of the North Pole's magnetic axis in the plane including the rotation axis and the magnetic axis, where the rotation axis is at the left-hand side of magnetic axis in the North Pole. Hence the polar angle $= 180^\circ$ is defined at the left-hand side of the magnetic axis. The angle between the magnetic axis and the rotation axis is chosen to be $< 90^\circ$, therefore the outgoing radiation from the South Pole can be detected with viewing angle $< 90^\circ$. In the South Pole, the emissions on the magnetic field lines emerging from polar angle larger (or smaller) than 180° produces the first (or second) peak. As shown in Fig. 5, the fractional thickness f becomes maximum around the polar angle of 200° , where $r_p(\phi_p)$ becomes minimum. Because larger fraction thickness f produces a stronger E_{\parallel} as equation (10) indicates, the emissions on the magnetic field lines emerging from $\sim 200^\circ$ is more stronger than those from $\sim 160^\circ$ and $\sim 240^\circ$. Consequently, third-peak-like structure is formed in the light curves of Fig. 4.

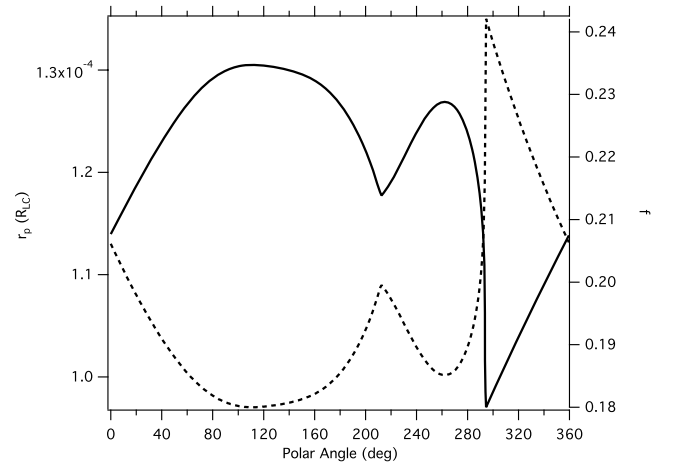


Figure 5. The distributions of the polar cap radius r_p (solid line) and the resultant f (dashed line) as a function of polar angles, with the vacuum dipole field. The definitions of the polar angle $= 0^\circ$ and 180° have been given in the text.

3.2.2 Gap thickness of the two layers

In the electrodynamic point of view, the thickness of the screening region of the gap, $h_2 - h_1$, will be determined by the photon–photon pair-creation rate between the γ -rays and X-rays from the stellar surface. It is expected that as the null charge surface is closer to the stellar surface, the number density of the X-ray photons increases in the gap and therefore the screening region becomes thinner. This indicates that the ratio of the thicknesses of the main acceleration region to the whole gap thickness, h_1/h_2 , is closer to unity as the null charge surface approaches the stellar surface. Because the radial distance to the null charge surface is a function of the azimuthal coordinate, it is expected that the ratio h_1/h_2 varies in the azimuthal direction. To simulate above dependency, let us assume the formula of the ratio as

$$\frac{h_1}{h_2}(\phi_p) = B_1 + B_2 \frac{1/r_{\text{null}}(\phi_p) - 1/r_{\text{null}}^{\max}}{1/r_{\text{null}}^{\min} - 1/r_{\text{null}}^{\max}}, \quad (23)$$

where the factor B_1 represents the ratio at the polar angle, at which the radial distance to the null charge surface becomes maximum, r_{null}^{\max} , and $B_1 + B_2$ corresponds to the ratio at azimuthal angle, at which radial distance to the null charge surface becomes minimum, r_{null}^{\min} . By fitting the spectral shape, we obtain $B_1 = 0.89$ and $B_2 = 0.09$.

To see the effects of the azimuthal dependency of the thickness ratio, h_1/h_2 , on the pulse profiles, Fig. 6 shows the simulated pulse profiles with equation (23) and the fixed fractional thickness of $f = 0.2$ and the number density of $1 - g_1 = 0.05$, which are the same with those of Fig. 3. By comparing Figs 3 and 6, one can see that the distribution of the h_1/h_2 does not affect much the light curves above energy $E > 1$ GeV, but it makes a bump in the bridge (~ 0.2 – 0.3 pulse phase) of the light curve around 100 MeV. We can see those light curves below $E < 1$ GeV in Fig. 6 are more consistent with the observation than those of Fig. 3. Wang et al. (2010) show that the ratio of the thicknesses h_1/h_2 affects the emissivity in the screening region. Because the particles in the screening regions, where the accelerating electric field is small, mainly produces the curvature photons of the energy less than $E \leq 1$ GeV, the azimuthal distributions of the thickness ratio affects the light curves $E \leq 1$ GeV.

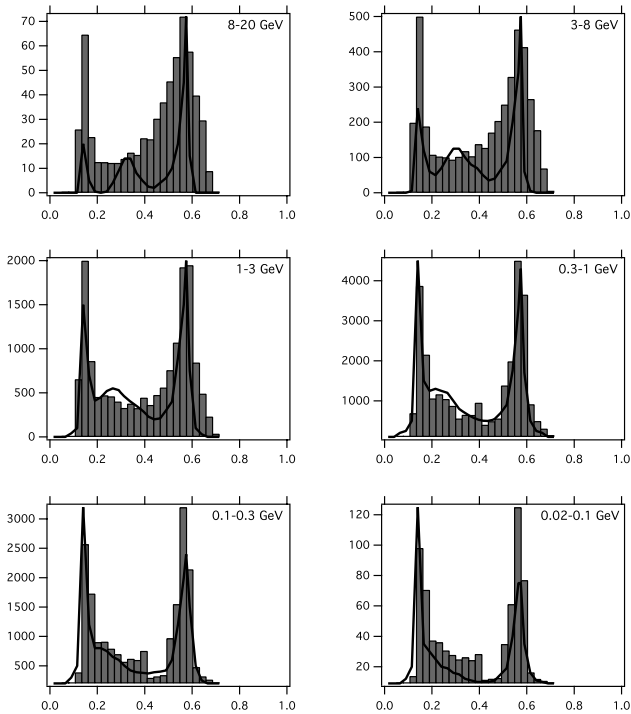


Figure 6. The energy-dependent light curves (histogram) with the distributions of h_1/h_2 provided by the three-dimensional outer gap. $1 - g_1$ and f are chosen as 0.05 and 0.2, respectively. The solid lines are the observed light curves from the *Fermi*-LAT (Abdo et al. 2010b).

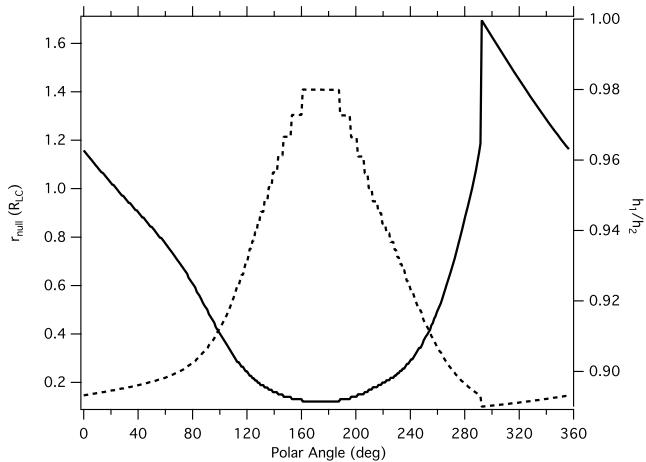


Figure 7. The distributions of the distance of the null charge surface from stellar surface (solid line) and the resultant h_1/h_2 (dashed line).

Fig. 7 shows the distributions of the radial distance to the null charge surface r_{null} (solid line) for the inclination angle $\alpha = 57^\circ$ and the corresponding h_1/h_2 (dotted line) expressed by equation (23). It shows that, at the polar angle $\sim 170^\circ$ that corresponds to pulse phase ~ 0.4 , the screening region is thinnest, which means the radiations below 1 GeV at the pulse phase ~ 0.4 are weaker than those of other pulse phases. Consequently, the shape of the bridge emissions of the light curves becomes more consistent with the observations and stands out the third-peak-like structure.

3.2.3 Number density

The azimuthal distribution of the particles will be more complicated, because it is related with (1) the motion of the particles under the Lorentz force and (2) the propagating direction of the curvature photons, which are eventually converted into the pairs in the gap. For example, the non-rotational electric field perpendicular to the magnetic field lines causes $\mathbf{E} \times \mathbf{B}$ drift motion of the particles. Moreover, because of the flight time of the photons and of the rotation of the magnetosphere, the magnetic field line, on which the pairs are created by the pair-creation process, is different from the field line, where the photons were emitted by the curvature radiation process.

With the two-dimensional two-layer model, Wang et al. (2010) found that the phase-averaged spectra for most of the γ -ray pulsars can be reproduced by the averaged charge density of $\bar{\rho}_0 \equiv [h_1\rho_1 + (h_2 - h_1)\rho_2]/h_2 \sim 0.5$. We want to point out that because the actual $E_\perp(\phi_p)$ is different at different ϕ_p , particles in different ϕ_p -cell may drift into other ϕ_p -cell. Therefore, we assume that the averaged charge density has a distribution in the azimuthal direction due to the effect of $E_\perp \times B$ drift motion. Without the effect of drifting, the number of particle in ϕ_p -cell is $N_0(\phi_p) \propto f(\phi_p)\bar{\rho}_0(\phi_p)$. With the drifting effect, the real number of particle in ϕ_p -cell $[N(\phi_p)]$ may come from $(\phi_p + \Delta\phi_p)$ -cell, i.e. $N(\phi_p) = N_0(\phi_p + \Delta\phi_p)$. Since the average charge density $\bar{\rho}(\phi_p) = N(\phi_p)/f(\phi_p)$, we obtain

$$\bar{\rho}(\phi_p) = \bar{\rho}_0 \frac{f(\phi_p + \Delta\phi_p)}{f(\phi_p)}, \quad (24)$$

where $\bar{\rho}_0 = 0.5$ is the averaged charge density without drift motion. It may be expected that displacement of the particles due to the drift motion becomes more important on the magnetic field line that has a smaller radial distance to the null charge surface, because the particles run longer distance in the outer gap, which is extending the null charge surface to the light cylinder. To take into account such effect, we may assume the formula of displacement as

$$\Delta\phi_p = F \frac{1/r_{\text{null}}(\phi_p) - 1/r_{\text{null}}^{\text{max}}}{1/r_{\text{null}}^{\text{min}} - 1/r_{\text{null}}^{\text{max}}}, \quad (25)$$

where F is a fitting parameter, which is chosen as -28° . We take $\Delta\phi_p = 0$ for $r_{\text{null}}^{\text{max}}$, because the null charge surface is close to the light cylinder, therefore particles from other cells cannot drift in. The negative value (that is, counter-direction of the rotation) of the displacement may be expected because (1) more particles are concentrated around the upper part of the gap and (2) the direction of the non-rotational electric field E_\perp is negative value at upper part of the gap, indicating the direction of the drift motion is counter-direction of the rotation.

Using the relationship between g_1, g_2 and h_1/h_2 given by equation (9) and $\bar{\rho} = [h_1\rho_1 + (h_2 - h_1)\rho_2]/h_2$, the distribution of $1 - g_1$ can be obtained. Fig. 8 is the energy-dependent light curves calculated using the azimuthal distribution of $1 - g_1$, where $h_1/h_2 = 0.927$ and $f=0.2$ are the same with those of Fig. 3. Compared with Fig. 3, it shows that the distribution of $1 - g_1$ makes a third peak at the bridge region (~ 0.3 pulse phase) when the energy > 1 GeV. This is due to the distribution of the number density in the main acceleration region, where the photons of $E > 1$ GeV are emitted. Fig. 9 shows the average charge density (filled circle) and the resultant charge density in the main acceleration region (circle). The average charge density and therefore the number density in the main acceleration region acquire the maximum value at polar angle around 240° , which corresponds to the pulse phase around 0.3.

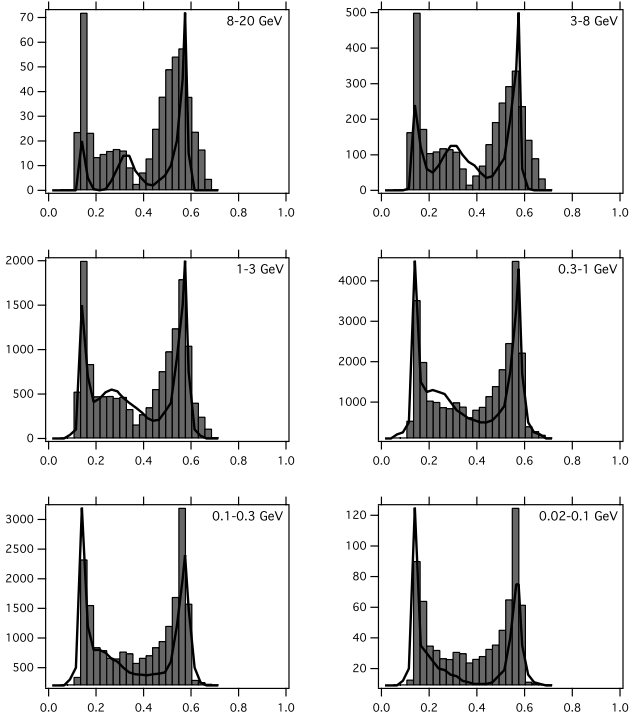


Figure 8. The energy-dependent light curves (histogram) with the distributions of $1 - g_1$ provided by the three-dimensional outer gap. h_1/h_2 and f are chosen as 0.927 and 0.2, respectively. The solid lines are the observed light curves from the *Fermi*-LAT (Abdo et al. 2010b).

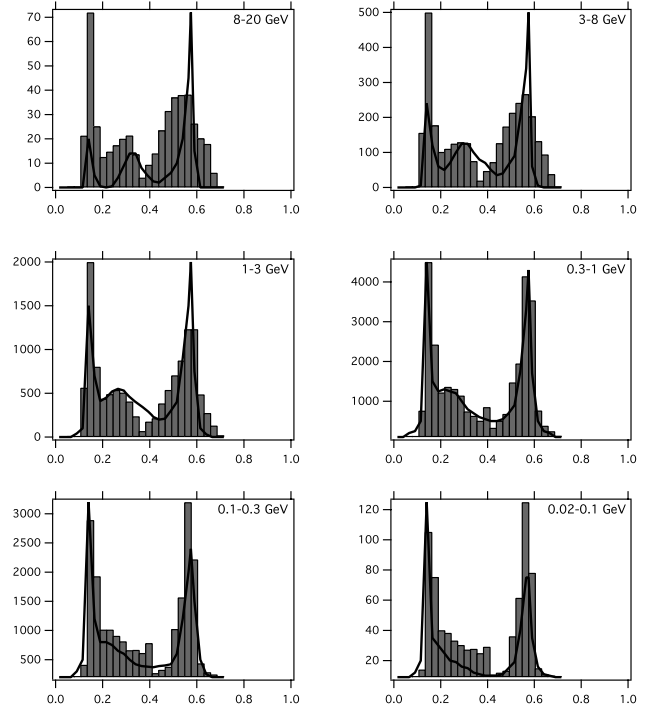


Figure 10. The energy-dependent light curves (histogram) with the distributions of $1 - g_1$, h_1/h_2 and f , provided by the three-dimensional outer gap. The solid lines are the observed light curves from the *Fermi*-LAT (Abdo et al. 2010b).

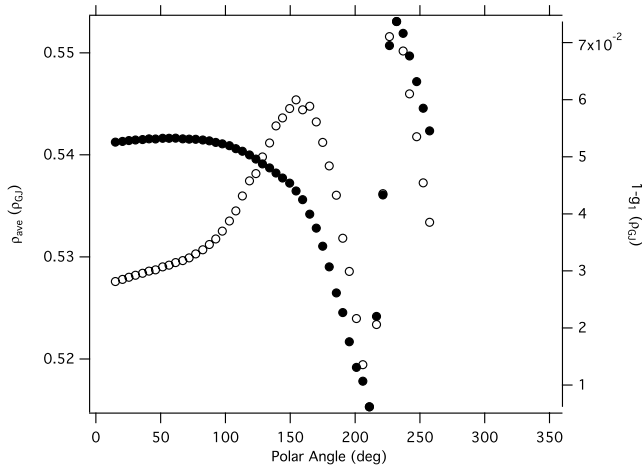


Figure 9. The distributions of the average charge density of the two layers (filled circle) and the resultant $1 - g_1$ (circle) of the fields of different polar angles.

3.3 Combined pulsed profile

We have discussed the effects of the distributions of f , h_1/h_2 and $1 - g_1$ on the shape of the energy-dependent light curves. As discussed in Section 3.2.2, the distribution of thickness ratio h_1/h_2 mainly affects the light curve of $E \leq 1$ GeV energy bands, and it makes a bump at pulse phase around 0.25 in the light curve below 1 GeV. The shape of bridge emission in the light curves above 1 GeV are mainly affected by the azimuthal distributions of the fractional thickness f and of the number density $1 - g_1$. We demonstrated that the third-

peak-like structure can be produced by the azimuthal structure of f , h_1/h_2 and $1 - g_1$.

Fig. 10 shows the pulsed profiles calculated by taking into account the azimuthal distributions for all f , h_1/h_2 and $1 - g_1$. We can see in Fig. 10 that there is a bump at the trailing part of the first peak in the pulse profile below 1 GeV, and it shifts towards the second peak in higher energy bands. Fig. 11 is the intensity map in the pulse phase and the energy plane. The darkness represents the number of the photons at the certain interval of the pulse phase. It shows that the third peak in the bridge region shifts towards the second peak as photon energy increases.

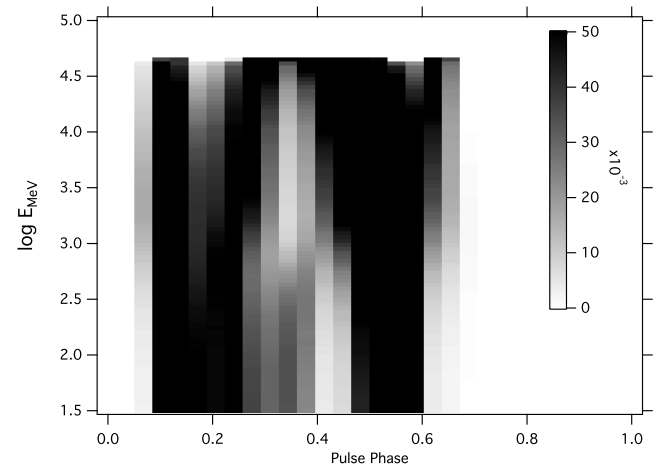


Figure 11. Intensity map in the pulse phase and energy plane. The darkness represents the percentage of the number of the photons of certain interval of pulse phase in the total number of photons of certain interval of energy.

The reason for the shift of the third peak is explained as follows. In the light curves in the energy bands lower than 1 GeV, the distributions of the thickness ratio h_1/h_2 make a third-peak structure at ~ 0.2 pulse phase. In the energy bands higher than 1 GeV, on the other hand, the azimuthal distribution of the fractional thickness, f , and the number density, $1 - g_1$, are more important, and they produce the third peak at ~ 0.3 – 0.35 pulse phase. Consequently, the differences in the standing phases of the third peak due to the distributions of h_1/h_2 and f (or $1 - g_1$) produce the shift of the third peak with the photon energy.

Here the distribution of the polar radius r_p , position of null charge surface r_{null} , which determine the distribution of $1 - g_1$, h_1/h_2 and f , depend on the inclination angle α . For instance, if the inclination angle is small, such as 10° , the shape of the polar cap is close to a circle, then the r_p of different polar angles are nearly a same value, the third peak made by it is not obvious. On the other hand, if the inclination angle is larger, the third peak made by the distribution of f is more obvious. In order to provide appropriate distributions of the three parameters, we use inclination angle $\alpha = 57^\circ$ and viewing angle $\beta = 80^\circ$.

The *Fermi* γ -ray telescopes have measured the γ -ray emissions from about 60 pulsars. However, the Vela pulsar is the only one showing the shifting third peak with energy. This may be because the Vela pulsar is relatively young and its gap thickness is smaller than other mature pulsars. For mature pulsars (e.g. the Geminga), the gap thickness will be much thicker ($f \sim 0.5$) than that ($f \sim 0.2$) of the Vela pulsar. In such a thick gap, the emissions from the different regions in the gap may smear out the effects of azimuthal structure of the gap. For the Crab pulsar, the gap thickness $f \sim 0.1$ is smaller than that of the Vela pulsar. However, the contributions of the inverse-Compton scattering from the secondary pairs, which are produced outside of the gap, dominate the emissions in γ -ray energy bands (Tang Anisia et al. 2008). This may be the reason that no third peak is observed in the light curves of the Crab pulsar.

3.4 Spectra

The spectral characteristics are summarized in Figs 12–15. Figs 12 and 13 compare the calculated (solid lines) and observed (filled circles) phase-averaged and phase-resolved spectra, respectively. By fitting calculated spectra with power law plus exponential cut-

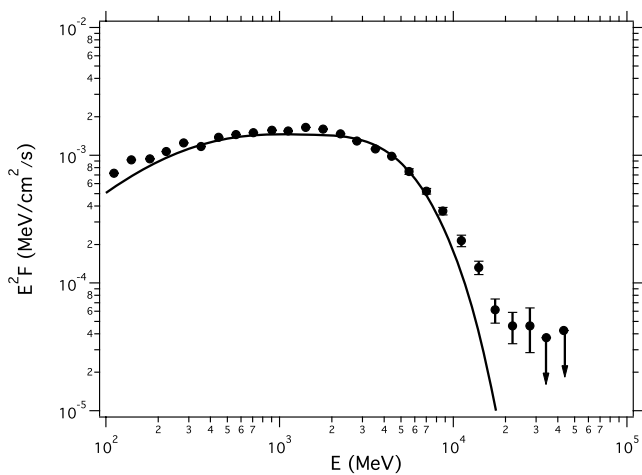


Figure 12. The phase-averaged spectrum with the distributions of $1 - g_1$, h_1/h_2 and f , comparing with the observed data (circle) from the *Fermi*-LAT (Abdo et al. 2010b).

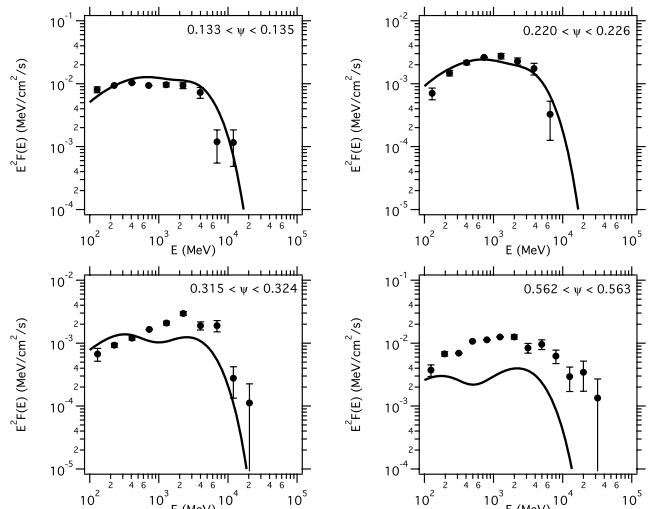


Figure 13. Four phase-resolved spectra provided by the more realistic model, using the distributions of $1 - g_1$, h_1/h_2 and f , and comparing with the observed data (circle) (Abdo et al. 2010b).

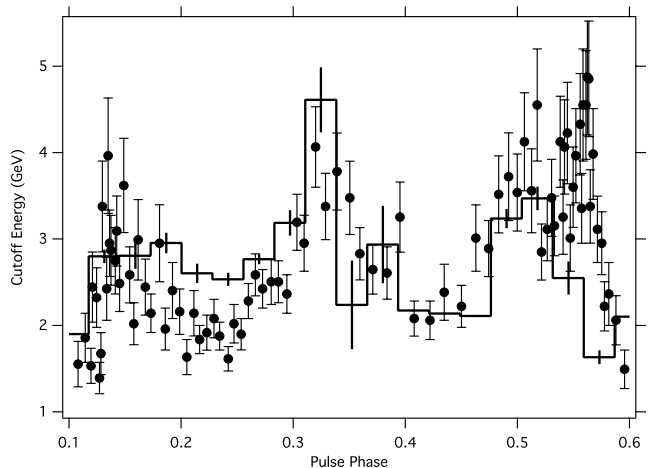


Figure 14. The cut-off energies of the phase-resolved spectra of different pulse phases given by the more realistic model, comparing with the observed data (circle) (Abdo et al. 2010b).

off form, Figs 14 and 15 show the cut-off energy and the photon index, respectively, as a function of the pulse phase.

As we can see from Fig. 14, the present model can explain the observed cut-off energy as a function of the pulse phase. This can be explained as the effect of the distribution of f , which decides the energies of the photons in the gap by determining the value of the accelerating electric field. And the cut-off energy of the spectrum is mainly determined by the emission from the main acceleration region. From Fig. 5, in the observable region from around 0° to 260° , there are three peaks of f , which correspond to the three peaks in Fig. 14. And the pulse phase of the middle peak in Fig. 14 is consistent with that of the third peak in the light curve made by the distribution of f . These two facts indicate that the distribution of f makes the calculated cut-off energies of the phase-resolved spectra consistent with the observed one.

Because the photon index is much more sensitive to the shape of the spectrum than the cut-off energy, Fig. 15 is not so consistent with the observation, where the photon indices between pulse phase of 0.3–0.5 are different with the observed ones. As the spectrum of

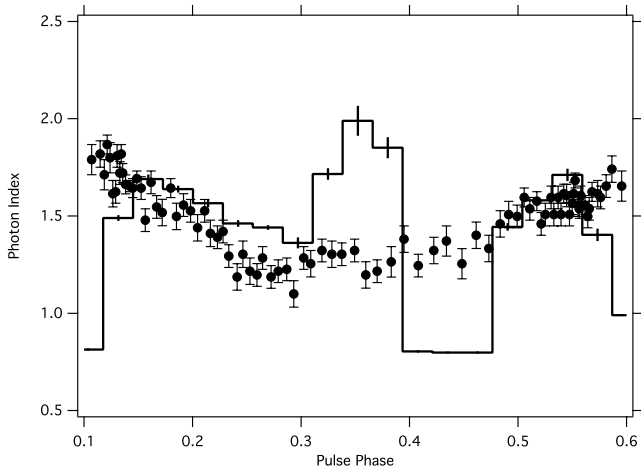


Figure 15. The photon indices of the phase-resolved spectra of different pulse phases given by the more realistic model, comparing with the observed data (circle) (Abdo et al. 2010b).

$0.315 < \psi < 0.324$ in Fig. 13 shows, the present model predicts a larger photon index at the pulse phase of 0.3–0.4 than the observations. For the pulse phase = 0.4–0.5, as we can see from the energy-dependent light curves (Fig. 10), the calculated photons are more than those of the observation. Consequently, the calculated curvature radiation from the main acceleration region is too strong, leading the calculated spectrum is hard with a photon index ~ 1 . For the other pulse phases, as shown in Fig. 13, the flux and the shape of the spectra are close to the observed ones, and the photon indices of these pulse phases can also explain the observed ones.

4 SUMMARY

In this paper, a three-dimensional outer gap model is built to explain the energy-dependent light curves of the Vela pulsar observed by the *Fermi*-LAT (Abdo et al. 2010b). In the present two-layer model, the acceleration and emission region in the gap consist of two parts, that is, the main acceleration region and the screening region. In the main acceleration region, the charge density is much lower than the Goldreich–Julian charge density and a strong electric field accelerates the particles to emit GeV photons via the curvature radiation process. In the screening region, the charge density is higher than the Goldreich–Julian charge density to screen out the accelerating electric field. We extend our two-dimensional two-layer model in Wang et al. (2010) into a three-dimensional one with the azimuthal structure of the fractional gap thickness (f), ratio of the thicknesses of the primary and whole region (h_1/h_2), and the number density in the main acceleration region ($1 - g_1$). Using constant $1 - g_1$, h_1/h_2 and f , although the calculated light curves

can qualitatively explain the observations of the Vela pulsar, the energy-dependent light curves cannot have the third peak. Therefore, we considered the possible azimuthal distributions of these three parameters. We found that the distributions of $1 - g_1$ and f make third-peak-like structure in the bridge region of light curve of above 1 GeV, while the distribution of h_1/h_2 makes a bump in the bridge region of the light curves below 1 GeV. We find that the phases of the third peaks caused by the azimuthal distributions of h_1/h_2 , $1 - g_1$ and f are different from each other. Consequently, the difference in the phases produces the shift of the combined third peak with the photon energy. We also showed that the present model can reproduce the distribution of the cut-off energy for each rotation phase.

ACKNOWLEDGMENT

We thank L. Zhang for useful discussion, and an anonymous referee for his useful suggestions. This work is supported by a GRF grant of the Hong Kong SAR Government under HKU700908P.

REFERENCES

- Abdo A. A. et al., 2010a, *ApJS*, 187, 460
 Abdo A. A. et al., 2010b, *ApJ*, 713, 154
 Arons J., 1983, *ApJ*, 266, 215
 Cheng K. S., Ho C., Ruderman M., 1986a, *ApJ*, 300, 500
 Cheng K. S., Ho C., Ruderman M., 1986b, *ApJ*, 300, 522
 Cheng K. S., Ruderman M., Zhang L., 2000, *ApJ*, 537, 964
 Daugherty J. K., Harding A. K., 1982, *ApJ*, 252, 337
 Du Y. J., Han J. L., Qiao G. J., Chou C. K., 2011, *ApJ*, 731, 2
 Dyks J., Rudak B., 2003, *ApJ*, 598, 1201
 Dyks J., Harding A. K., Rudak B., 2004, *ApJ*, 606, 1125
 Fang J., Zhang L., 2010, *ApJ*, 709, 605
 Goldreich P., Julian W. H., 1969, *ApJ*, 157, 869
 Harding A. K., Usov V. V., Muslimov A. G., 2005, *ApJ*, 622, 531
 Harding A. K., Stern J. V., Dyks J., Frackowiak M., 2008, *ApJ*, 680, 1378
 Hirotani K., 2008, *ApJ*, 688, L25
 Romani R. W., 1996, *ApJ*, 470, 469
 Ruderman M. A., Sutherland P. G., 1975, *ApJ*, 196, 51
 Takata J., Chang H. K., 2009, *MNRAS*, 392, 400
 Takata J., Shibata S., Hirotani K., 2004, *MNRAS*, 354, 1120
 Takata J., Chang H.-K., Cheng K. S., 2007, *ApJ*, 656, 1044
 Takata J., Chang H. K., Shibata S., 2008, *MNRAS*, 386, 748
 Takata J., Wang Y., Cheng K. S., 2010, *ApJ*, 715, 1318
 Tang Anisia P. S., Takata J., Jia J. J., Cheng K. S., 2008, *ApJ*, 676, 562
 Wang Y., Takata J., Cheng K. S., 2010, *ApJ*, 720, 178
 Yadigaroglu I. A., 1997, PhD thesis, Stanford Univ.
 Yadigaroglu I. A., Romani R. W., 1995, *ApJ*, 449, 211
 Zhang L., Cheng K. S., *ApJ*, 1997, 487, 370
 Zhang L., Cheng K. S., 2001, *MNRAS*, 320, 477

This paper has been typeset from a $\text{\TeX}/\text{\LaTeX}$ file prepared by the author.